JASA ARTICLE

Traveling wave thermoacoustic refrigeration with variable phase-coordinated boundary conditions

Jesse Callanan,[a] Revant Adlakha, Mohamed Mousa, and Mostafa Nouh[b]
Department of Mechanical and Aerospace Engineering, University at Buffalo (SUNY), Buffalo, New York 14260-4400, USA

ABSTRACT:
Thermoacoustic refrigerators exploit the thermodynamic interaction between oscillating gas particles and a porous solid to generate a temperature gradient that provides a cooling effect. In this work, we present a resonator with dual enclosed driver end-caps and show that the temperature gradient across a ceramic thermoacoustic element placed in the cavity could be controlled by modifying the phase difference of the drivers, thus enabling precise control of the refrigeration capability via the temperature difference. Through DELTAEC simulation results, the response of the temperature gradient to various dynamic boundary conditions that alter the time-phasing and wave dynamics in the resonator are demonstrated. An experimental apparatus is constructed with two moving-coil speakers and a ceramic stack, which is shown to exhibit a temperature gradient along its length, based on the traveling-wave-like nature of the acoustic wave excited by the speakers. By adjusting the relative phase lag between the two speakers, the temperature gradient across the stack is made to increase, decrease, or flip sign. Finally, a desired temperature difference that changes in time is achieved. The results presented in this work represent a key conceptual advancement of thermoacoustic-based temperature control devices that can better serve in extreme environments and precision applications. © *2023 Acoustical Society of America*. https://doi.org/10.1121/10.0023954

(Received 11 May 2023; revised 26 October 2023; accepted 29 November 2023; published online 26 December 2023)
[Editor: David E. Scarborough] Pages: 3943–3954

I. INTRODUCTION

Thermoacoustic refrigeration devices have been of interest for several decades, with applications ranging from cooling of electronic parts[1] to large-scale industrial processes.[2,3] Thermoacoustic refrigerators (TARs) rely on the thermodynamic interaction between moving air particles and a solid porous medium to generate a steep temperature gradient, which allows these devices to act as robust heat pumps with few moving parts, no sliding seals, and without the need for specialty materials like semiconductors.[4–7] TARs are attractive options for remote settings (such as aboard spacecraft[8]) due to their simple and robust operating mechanisms and low level of induced mechanical vibration (compared to many rotary systems). They also represent an environmentally friendly alternative to traditional cooling systems because they do not require refrigerants or other chemicals.

One exciting early example of a TAR used in practice was the Space ThermoAcoustic Refrigerator (STAR), which utilized an electrodynamic loudspeaker to generate a 400 Hz sound wave within a closed quarter-wavelength resonator. The wave interacted with a polyester film porous cylindrical stack and generated a temperature gradient such that the cold side was 0.8 times the temperature of the hot side at a heat load of 2 W.[8] Earlier work presented by Hofler showed that a conceptually similar design achieved a temperature ratio of 0.66; this work also provided extensive analysis and characterization of the system performance.[9] More recently, thermoacoustic cryocooling has found application in the James Webb Telescope,[10–12] where a dual driver pulse tube is utilized to create a standing wave in a resonator that is embedded with heat exchangers made of thin metal sheets to help in the cooling process of the onboard Mid-InfraRed Instrument (MIRI) camera. A comprehensive description of thermoacoustic engines in general, including thermoacoustically-driven refrigerators, was given by Swift,[13] along with a highly instructive one-dimensional theoretical framework (based on Rott's linear theory) and overview of experimental considerations.[14]

Since these foundational efforts have established the primary operating principles of TARs, additional features have been incorporated to improve the overall performance or realize new functionalities in TARs. Raspet *et al*. showed that the performance of a TAR depends strongly on the acoustic standing wave ratio. The highest coefficient of performance was achieved when there was a significant traveling-wave component in the refrigerator,[15] which confirmed earlier results presented by Hofler.[16] Several papers have investigated the performance of thermoacoustic engines—prime movers used to generate sound waves from heat—under active control schemes[17–19] and piezoelectric coupling.[20–25] Acoustic oscillations in small-scale thermoacoustic resonators are typically standing waves that exhibit a pressure-velocity time-phasing that is detrimental to the

[a]Also at: Materials and Physics Applications Division, Center for Integrated Nanotechnologies, Los Alamos National Laboratory, Los Alamos, NM 87544-0600, USA.
[b]Also at: Department of Civil, Structural and Environmental Engineering, University at Buffalo (SUNY), Buffalo, NY 14260-4300, USA. Email: mnouh@buffalo.edu.

acoustic power output of conventional systems.[26] Actively controlled thermoacoustic devices that excite hybrid standing/traveling waves by sensitively tuning this phasing have been recently shown to increase the amount of extractable acoustic power in such engines.[27]

These concepts are of key interest for TAR applications as well. For example, Shearer and Hofmann demonstrated a method to control the driving frequency of a TAR such that it is optimized to maintain the resonance frequency of the acoustic system without the need for external sensors.[28] Poignand *et al.* generated optimal acoustic fields for refrigeration in a highly compact form factor using multiple transducers; their work showed that the optimal acoustic field differed significantly from a traditional standing acoustic wave.[29] Ramadan *et al.* developed and tested a compact TAR that utilized two electroacoustic transducers to achieve improved performance.[30] Their results show significantly improved specific cooling capacity overall and an optimal transducer phasing, which was in good agreement with the numerical model. Recent work by Chen and Xu showed that the direction of heat flow through the porous material was altered when two controlled drivers were utilized in an annular shaped thermoacoustic engine, and the temperature difference was dependent on the resonating frequency of the system.[31] Widyaparaga *et al.* showed experimentally that a dual acoustic driver configuration could yield controlled acoustic power flow and standing/traveling-wave dynamics with good refrigeration performance and that the system could be used for heating or cooling by altering the control transducer phasing.[32,33]

In this work, we more closely investigate the acoustic wave dynamics to better understand the influence of the relative driving phase difference between a pair of transducers in refrigeration applications. Both simulation and experimental results are presented that demonstrate the utility of actively controlling the boundary conditions (i.e., the transducers) for increasing the temperature gradient across the thermoacoustic element and thereby increasing the system's refrigeration capacity. The capability to control the temperature in real time using the dynamic transducer boundaries is demonstrated theoretically by computing key acoustic wave metrics such as the wave eccentricity, as well as experimentally. The relationships established at the beginning of this work are shown to be crucial for enabling control of both the temperature gradient magnitude and direction. The novel capability of adjusting acoustic power flow opens the door to wide-ranging applications in more precise temperature control and refrigeration functions, such as improved sensor stability in extreme environments and environmentally friendly localized cooling.

II. THEORETICAL MODELING

Arguably the most influential mathematical description of an acoustic system with longitudinal temperature variations was derived by Nikolaus Rott in 1969[34] and popularized by Greg Swift in the early 1990s.[13,14] The model will be employed using the computer program DELTAEC. The key variables are the acoustic pressure, $p(x,t) = p_1(x)e^{-i\omega t}$, the gas particle volume velocity, $v(x,t) = v_1(x)e^{-i\omega t}$, the total energy, $\dot{H}(x)$, and the temperature, $T(x)$. The pressure and velocity spatial functions are complex, $p_1(x) \in \mathbb{C}$ and $v_1(x) \in \mathbb{C}$, while the energy and temperature are real.

A. Standing wave ratio and wave eccentricity

The pressure waveform can be represented as a sum of complex exponentials,

$$p(x,t) = e^{-i\omega t}\left(W_+ e^{ikx} + W_- e^{-ikx}\right), \tag{1}$$

where ω is the frequency of oscillation, k is the wavenumber, and under nondispersive assumptions, the speed of sound satisfies $c = \omega/k$. The complex coefficients W_+ and W_- define the amplitude and phase of a leftward- and a rightward-traveling wave, respectively, which are superimposed to realize the total pressure wave, $p(x,t)$. The frequency of oscillation, ω, depends on the excitation source or the tube length.[35] The complex wave amplitude terms W_+ and W_- depend on the boundary conditions and the excitation source: if the tube is infinitely long, $W_+ = 0$ because there are no reflections and no wave can travel in the $-x$ direction. If the tube is rigidly closed at both ends, $|W_+| = |W_-|$ and the two traveling-wave components have equal amplitudes; the result is a perfect standing wave.

In a pure standing wave, the net output power is zero because the acoustic pressure and particle velocity are out of phase:[36] i.e., the wave can do no work because the force and motion are not synchronized. Previous studies have shown that traveling-wave TARs are more capable than standing-wave engines, and therefore it is desirable to generate a traveling wave to improve the refrigeration performance of the system. One method to quantify the wave as either standing, traveling, or something in between is the wave eccentricity.[27] The eccentricity is defined as

$$e_c = \frac{|W_+| - |W_-|}{|W_+| + |W_-|}. \tag{2}$$

The eccentricity, e_c, is named as such because it is proportional to the eccentricity of the ellipse traced by the sum of the complex phasors W_+ and W_- as the position in space is varied at one time instant.[27,37] It is important to note that this definition of ellipse eccentricity is nonstandard, but it is very well suited to this application. Typically, eccentricity increases as a circle is "squished": i.e., the eccentricity of a perfect circle is zero, and a parabola has eccentricity of unity. In this work, we define the eccentricity to be the ratio of the semi-minor to semi-major axis, which gives a value of unity for a perfect circle (pure traveling wave) and a value of zero when the ellipse degenerates into a line (standing wave) because this definition has been frequently used in previous literature pertaining to this topic area.[27,37] The end goal of this work is to experimentally demonstrate that controlling the relative phase of the

https://doi.org/10.1121/10.0023954

velocities of the resonator boundaries can increase the magnitude of the wave eccentricity, e_c, generating a traveling wave (or dynamics that are more traveling-wave-like) in the system. Increasing the eccentricity changes the temperature difference, thereby improving the refrigeration capabilities of the system through boundary condition control.

B. Eccentricity computation

The wave eccentricity can be computed online, as demonstrated by Bucher,[37] but in the case of limited spatial sensing capabilities (i.e., only a few available microphones), it can be also computed offline using a gradient based optimization with a set of time-series data. For a set of N_s microphones, in one experimental trial there are N_t data points collected at each sensor. To find the eccentricity, the ideal sinusoidal pressure waveform,

$$\begin{aligned}\hat{p}(x,t) &= \mathrm{e}^{-\mathrm{i}\hat{\omega}t}\hat{W}(x)\\ &= \mathrm{e}^{-\mathrm{i}\hat{\omega}t}\left(\hat{W}_{+}\mathrm{e}^{\mathrm{i}\hat{k}x}+\hat{W}_{-}\mathrm{e}^{-\mathrm{i}\hat{k}x}\right),\end{aligned} \tag{3}$$

must be determined, where $\hat{(\cdot)}$ indicates an estimated quantity that will result from a curve fitting operation with Eq. (3) as the model. For example, $\hat{p}(x,t)$ is the estimated version of $p(x, t)$, and so on. Additionally, the notations $(\cdot)_{\mathrm{sim}}$ and $(\cdot)_{\mathrm{exp}}$ will henceforth be used to denote simulated and experimental quantities, respectively.

C. DELTAEC model description

DELTAEC is a physics simulation software made available for free from Los Alamos National Laboratory.[38,39] A model of the thermoacoustic system under investigation in this work was developed using DELTAEC, and an overview of the model is shown in Fig. 1. The system under consideration is referred to as a thermoacoustic refrigerator with dual-electroacoustic actuators (TARDE). The TARDE DELTAEC model consists of 16 segments, including components such as resonators, ducts, and thermoacoustic elements, as well as individual segments that represent mathematical operations on the state variables. The segments can be seen in the schematic view in the bottom of Fig. 1. The segments represent the following, from left to right: 0, a rigid cap for the BEGIN segment; 1, a thermal anchor segment; 2, a short length of duct; 3, a moving-coil speaker (actuator *A*); 4, a conical section; 5, a small diameter duct; 6, a math segment to compute the pressure velocity phasing; 7, a segment to represent the material surrounding the stack; 8, a square-pore thermoacoustic stack; 9, a math segment to compute the temperature difference across the stack; 10, a short length of steel duct; 11, an anchor; 12, a long polycarbonate resonator duct; 13, a conical section; 14, another moving-coil speaker (actuator *B*) with 15, a short length of duct; and finally, 16, a rigid cap. The guesses and targets are summarized in the lower table: the guesses are initial pressure magnitude and phase at the BEGIN segment, and the targets are zero real and imaginary acoustic impedance at the rigid cap HARDEND (segment 16). The DELTAEC system model as described amounts to solving the following problem: For a given input voltage magnitude and phase to each speaker, what are the resulting pressure magnitude and phase that will satisfy the zero-particle velocity condition at the right-most rigid cap? The zero velocity condition at the left-most rigid cap, near speaker *A*, is satisfied intrinsically by forcing zero velocity there. Once the impedance conditions are

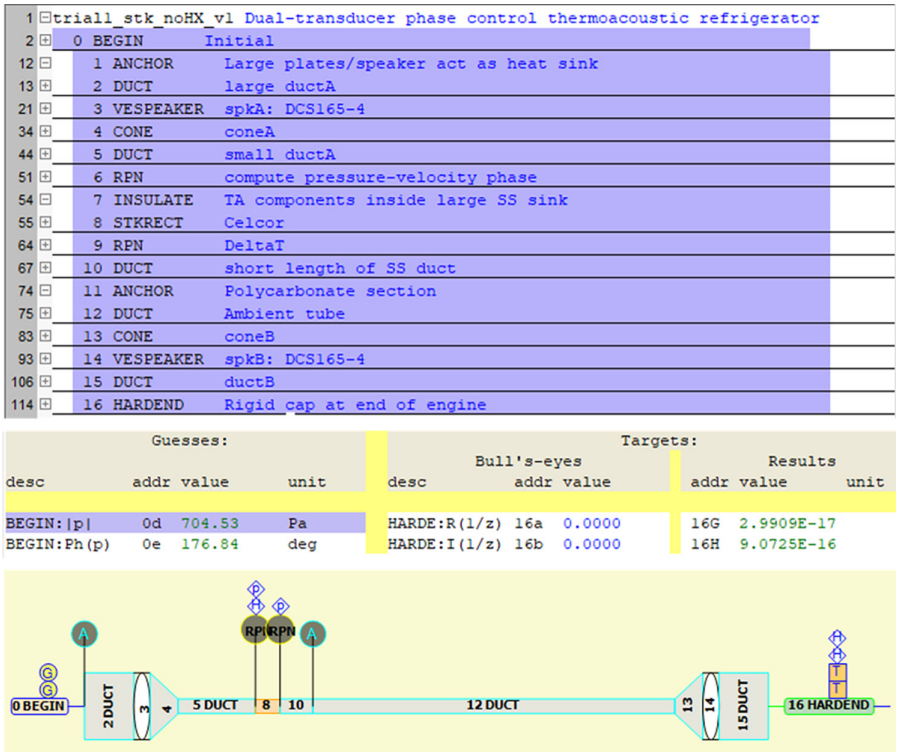

FIG. 1. (Color online) Overview of the DELTAEC model for a thermoacoustic refrigerator with dual-electroacoustic actuators (TARDE).

satisfied, the state variables along the engine are known and the refrigeration performance can be analyzed.

The variables of interest for this work are the complex acoustic pressure, $p_{\mathrm{DEC}}(x,0)$, computed via DELTAEC, which is returned as a spatial amplitude, and the temperature at each end of the stack, $T_{1,\mathrm{sim}}$ and $T_{2,\mathrm{sim}}$. The complex pressure amplitude returned by DELTAEC is "animated" in time so that it can be directly used in the fitting procedure described in Sec. II B. The full simulated pressure waveform then becomes

$$p_{\mathrm{sim}}(x,t) = \mathrm{e}^{-\mathrm{i}\omega t} p_{\mathrm{DEC}}(x,0), \tag{4}$$

where the time array, t, matches that of the experimental runs. p_{sim} can be fed directly into the eccentricity computation optimization algorithm for a direct comparison with the experimental data.

III. EXPERIMENTAL APPARATUS

The TARDE experimental apparatus consists of a thermoacoustic stack (porous medium) coupled to a resonator tube and two large-diameter moving-coil speakers. A schematic of the system is shown in Fig. 2(a). The thermoacoustic stack, located at x_s, is square-pore Celcor ceramic substrate (Corning Environmental Products Division, Corning, NY) with $y_0 = 1$ mm pore size, $\ell_0 = 0.5$ mm pore wall thickness, and length of $L_s = 50$ mm located at $x_s = 470$ mm. The stack is housed in a section of thick-walled stainless steel tubing to minimize unwanted heat conduction along the length of the stack. The thick-walled stainless steel tubing is connected to two resonator sections: to the left, a short length of thin-walled stainless steel, and to the right, a longer polycarbonate section. At the ends of each resonator section are identical electro-acoustic actuator elements (moving-coil speakers with fixed permanent magnets) and an additional section of polycarbonate tubing, which encloses the speakers. By matching the air pressure behind the speaker, the diaphragm experiences zero net-force and can operate as efficiently as possible.

The TARDE apparatus is equipped with two thermocouples firmly pressed against the stack at both sides, as shown in Fig. 2(b). The thermocouples measure the local temperature at those locations. The thermocouple signals were read with an NI USB6341 data acquisition device (DAQ). The system is also equipped with four microphones ($N_s = 4$), 1/4 in. prepolarized BSWA MP471S IEC61672 Class 1 with a 6 Hz to 40 kHz dynamic range and a 0.5 mV/Pa sensitivity attached to BSWA MA401 ICP preamplifiers (BSWA, Beijing, China). The microphone signals were read using a BSWA MC3242 DAQ. In the following sections, the experimental pressure signal, $p_{\mathrm{exp}}(x_n, t_m)$, denotes the (real) acoustic pressure amplitude measurement at the n^{th} microphone and the m^{th} time step.

The speaker control signals were generated in MATLAB and sent to the NI USB6341 DAQ and subsequently to two independent audio amplifiers, which drove the speakers. The amplifiers were tuned to maintain the same output sound pressure level to ensure identical amplitude contributions were maintained across the two drivers. The MATLAB script was initialized with the two DAQs and time-synced to ensure the microphone signals were synchronized with the temperature readings and driver signals. The audio signals to the secondary (x_B) driver were delayed with respect to the primary (x_A) driver by adding a phase shift, which varied across trials as indicated. The NI USB6341 DAQ and

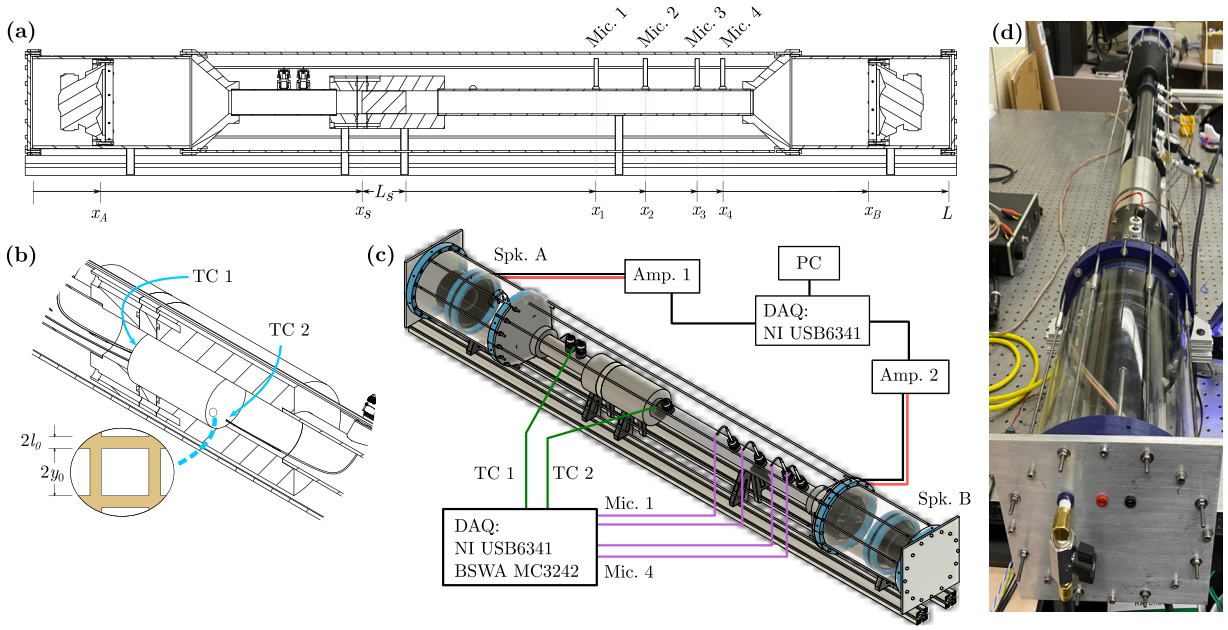

FIG. 2. (Color online) (a) To-scale drawing of the experimental TARDE apparatus showing relevant dimensions and microphone positions. (b) Close-up view showing stack with key geometrical definitions and the placement of thermocouples 1 (TC 1) and 2 (TC 2). (c) Three-dimensional (3D) schematic diagram with data acquisition equipment including audio signal output and amplifiers. (d) Actual photo of the experimental setup.

https://doi.org/10.1121/10.0023954

BSWA MC3242 DAQ are set to record and playback audio at a sampling frequency of 51.2 kHz. The data collection process was automated over the parametric phase delays using the MATLAB script. The two DAQs were initialized in the script using the DAQ toolbox, and an aggregate DAQ was formed by adding specific input and output channels to the digital device, enabling time synchronization across multiple devices. The two speakers were driven with their specific signals for 45 s, based on the appropriate amplitudes and phase angle. Simultaneously, the audio from the four microphones and the raw thermocouple readings were recorded. To ensure that the temperature across the stack was the same at the start of each test, the thermocouples measured the temperature for 30 s, and if the difference of the mean of the temperature readings was below a threshold (set at 0.4 °C) the next trial started. A convection fan was used to assist the cooling process, which was automatically turned on while the script waited for the system to cool down.

IV. RESULTS AND DISCUSSION

A. Experimental data collection

In Fig. 3, the raw microphone recordings from the four microphones are shown in both time and frequency domains for two speaker delay phases, $\phi = -75^\circ$ and $\phi = 60^\circ$, with an excitation frequency of 100 Hz. Figures 3(a) and 3(d) show the microphone recordings for $\phi = -75^\circ$ and $\phi = 60^\circ$, respectively, for the first 1 s, and Figs. 3(b) and 3(e) show the zoomed-in version of the microphone signals. It is evident from the change in amplitudes of the signal from each microphone that the pressure inside the tube at the microphone locations changes as a function of the relative phase of the two speakers: i.e., the amplitude measured by microphone 4 in Fig. 3(e) is much lower than that in Fig. 3(b). Figures 3(c) and 3(f) show the power spectrum of the microphone signals for $\phi = -75^\circ$ and $\phi = 60^\circ$, respectively. The power spectrum shows the presence of the fundamental mode (100 Hz, which is also the driving frequency) and higher harmonics (200, 300, 400 Hz) of the fundamental mode. It can be observed that while the harmonics remain the same within various cases, their magnitudes vary as the driver phase angle is changed.

Figure 4 shows the raw temperature readings for the two sensors as the relative driver phase is varied. The purpose of the results presented in Fig. 4 is to show the transience of the thermocouple readings and the ability of the TAR to switch the sign of the temperature gradient (i.e., swap the hot and cool sides) by varying the relative driver phase difference. The light gray and dark gray points denote the raw thermocouple readings for T_1 and T_2, respectively. The raw data were low pass filtered to remove the noise and are plotted as red and blue lines for T_1 and T_2, respectively. The raw temperature signals were recorded for a total of 45 s to ensure a steady state was achieved. Figure 4(a) shows the temperature signals for a relative driver phase of $\phi = -60^\circ$. In this case, the near side (T_1) became cooler than the ambient temperature (25 °C) while the far side (T_2) became hotter, as shown in Fig. 4(a), giving an overall temperature difference of $\Delta T = T_1 - T_2 = -2$ °C. Figure 4(b) shows the temperature signals for a relative driver phase of $\phi = 60^\circ$. The near side (T_1) shows a significant decrease from the ambient temperature, while the far side (T_2) shows a significant increase leading to a temperature difference of $\Delta T = -10$ °C. Finally, for a relative phase difference of $\phi = 180^\circ$ [Fig. 4(c)] an inverted behavior is seen: the far

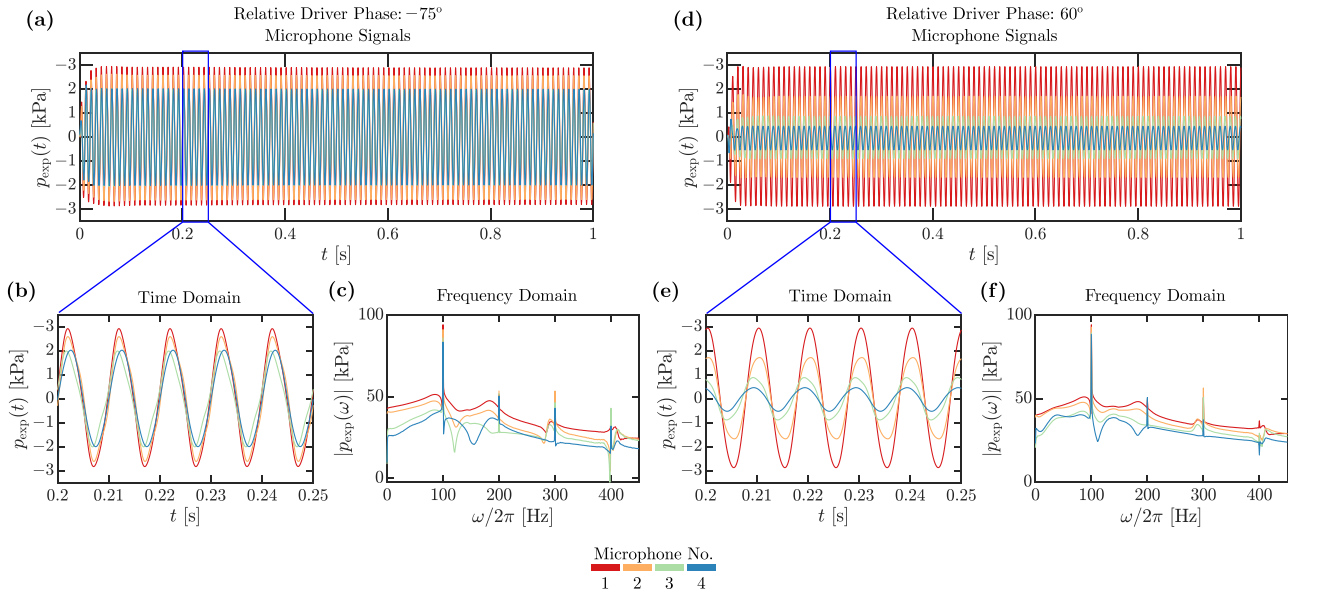

FIG. 3. (Color online) Raw microphone signals in the time and frequency domains. (a) and (d) show the first one second of raw microphone signals for $\phi = -75^\circ$ and $\phi = 60^\circ$, respectively. (b) and (e) show close-ups of raw microphone signals for $\phi = -75^\circ$ and $\phi = 60^\circ$, respectively. (c) and (f) show the power spectrum of the raw microphone signals for $\phi = -75^\circ$ and $\phi = 60^\circ$, respectively.

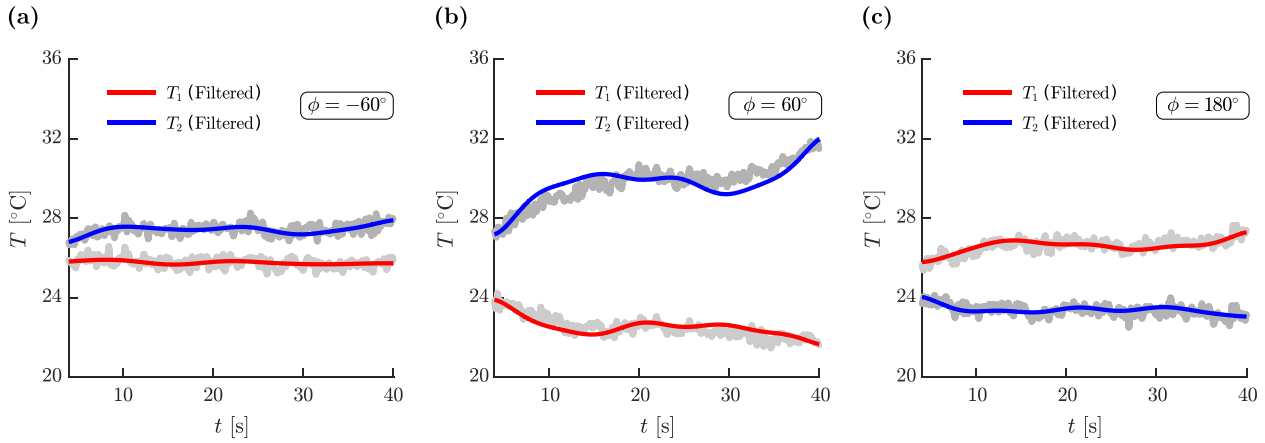

FIG. 4. (Color online) Temperature readings for various relative driver phases. (a) shows the temperature variation for the two temperature sensors for $\phi = -60°$. (b) shows the temperature variation for the two temperature sensors for $\phi = 60°$. (c) shows the temperature variation for the two temperature sensors for $\phi = 180°$. The light and dark gray points show the raw thermocouple readings, while the red and blue lines show the filtered temperature values for near-side (T_1) and far-side (T_2), respectively.

side (T_2) shows a decrease from the ambient temperature, while the near side (T_1) shows an increase leading to a temperature difference of $\Delta T = 4\,°\mathrm{C}$.

B. Data fitting

The DELTAEC simulation results were computed as waveform amplitudes with arbitrary time phasing,[38] so the absolute time phasing can be adjusted to match that of the experiment. This was achieved by computing the optimal time phase adjustment, Φ, such that the errors between the simulation signals and the experimental data were minimized. The adjusted space-time simulation signal, $\bar{p}_{\mathrm{sim}}(x,t)$, is obtained from the DELTAEC pressure data as

$$\begin{aligned}\bar{p}_{\mathrm{sim}}(x,t) &= a_1 \mathrm{e}^{-\mathrm{i}\Phi} p_{\mathrm{sim}}(x,t) \\ &= a_1 \mathrm{e}^{-\mathrm{i}(\omega t+\Phi)} p_{\mathrm{DEC}}(x,0)\end{aligned} \tag{5}$$

by introducing a time-phase adjustment, Φ, and an amplitude adjustment, a_1. The latter accounts for slight differences in the speaker's driving amplitude for different phase cases, potentially due to changing tube dynamics or imperfect speaker motion. Both Φ and a_1 are unknown and are chosen to synchronize $p_{\mathrm{exp}}(x,t)$ and $\bar{p}_{\mathrm{sim}}(x,t)$ by minimizing the cost function

$$J_{\mathrm{sync}} = \sum_{n=1}^{N_s}\sum_{m=1}^{N_t} |p_{\mathrm{exp}}(x_n,t_m) - \Re\{\bar{p}_{\mathrm{sim}}(x_n,t_m)\}|. \tag{6}$$

Once the simulated pressure is amplitude and phase-synced with the experimental pressure, traveling-wave components can be estimated, yielding $\hat{\bar{p}}_{\mathrm{sim}}$, which is the estimated version of $\bar{p}_{\mathrm{sim}}$, as

$$\hat{\bar{p}}_{\mathrm{sim}}(x,t) = \mathrm{e}^{-\mathrm{i}\hat{\omega}t}\hat{W}_{\mathrm{sim}}(x), \tag{7}$$

where $\hat{W}_{\mathrm{sim}} = \hat{W}_{+,\mathrm{sim}}\mathrm{e}^{\mathrm{i}\hat{k}x} + \hat{W}_{-,\mathrm{sim}}\mathrm{e}^{-\mathrm{i}\hat{k}x}$ and $\hat{W}_{\pm,\mathrm{sim}}$ denotes the estimated backward and forward complex coefficients, which would be later used to compute the wave eccentricity for the DELTAEC simulations. The parameters $\hat{W}_{\pm,\mathrm{sim}}$, $\hat{k}$, and $\hat{\omega}$ can be estimated by minimizing the cost function

$$J_{\mathrm{sim}} = \sum_{n=1}^{N_s}\sum_{m=1}^{N_t} |\bar{p}_{\mathrm{sim}}(x_n,t_m) - \hat{\bar{p}}_{\mathrm{sim}}(x_n,t_m)|. \tag{8}$$

In the experimentally obtained data, the operational frequency, ω, is known because it is the same as the driving frequency, and under nondispersive assumptions, the wavenumber, k, is known as well, but as a check they will be included as optimization variables. Including the wavenumber and frequency as optimization variables allows the data fitting procedure to account for small variations in the experimental conditions and will confirm the simplifying assumptions made in the acoustic model. Therefore, the estimated complex coefficients $\hat{W}_{+,\mathrm{exp}}$ and $\hat{W}_{-,\mathrm{exp}}$, temporal frequency, $\hat{\omega}$, and spatial frequency, $\hat{k}$, must be determined, and the cost function to be minimized is

$$J_{\mathrm{exp}} = \sum_{n=1}^{N_s}\sum_{m=1}^{N_t} |p_{\mathrm{exp}}(x_n,t_m) - \Re\{\hat{p}_{\mathrm{exp}}(x_n,t_m)\}|. \tag{9}$$

$\Re\{\hat{p}_{\mathrm{exp}}(x_n,t_m)\}$ is the real part of the estimated (complex-valued) pressure amplitude, and the sum is taken over all N_s sensor locations and N_t time steps. Because the coefficients $\hat{W}_{\pm,\mathrm{exp}}$ are complex, the optimization process as coded in MATLAB considers the real and imaginary parts separately when computing $\hat{p}_{\mathrm{exp}}$. The error metric Δ can then be defined as

$$\Delta = \frac{\sum_{n=1}^{N_s}\sum_{m=1}^{N_t} |p_{\mathrm{exp}}(x_n,t_m) - \Re\{\hat{\bar{p}}_{\mathrm{sim}}(x_n,t_m)\}|}{N_s N_t \max\{p_{\mathrm{exp}}\}} \times 100, \tag{10}$$

which represents the mean difference between the simulation and experimental measurement normalized by the

https://doi.org/10.1121/10.0023954

maximum experimentally measured acoustic pressure, expressed as a percentage. It is important to note that Δ is evaluated only for the N_s experimentally obtained points at the x_n locations. It captures the discrepancy between the waveform with the mathematical form of Eq. (7) and the experimental data. This error is the most important for comparing the wave eccentricity between the two cases. However, it is also of interest to consider the error accumulated by fitting the mathematically ideal waveform to each data set independently. For example, for the experimental data, this error metric is defined as

$$\delta_{\text{exp}} = \frac{\sum_{n=1}^{N_s}\sum_{m=1}^{N_t} |p_{\text{exp}}(x_n,t_m) - \Re\{\hat{p}_{\text{exp}}(x_n,t_m)\}|}{N_s N_t \max\{p_{\text{exp}}\}} \times 100, \quad (11)$$

which takes the same form as the error metric Δ but emphasizes the error due to the experimental data fitting only. Similarly to Eq. (11), an error metric, δ_{sim}, can be defined, which quantifies the estimation error between $\bar{p}_{\text{sim}}$ and $\hat{\bar{p}}_{\text{sim}}$. The optimized fit parameters for the DELTAEC simulation and the results from fitting an ideal sinusoid waveform to the experimental data are shown in the supplementary material in Table I. The small variation in the wavenumber k between trials indicates that a more advanced acoustic model would be able to better fit the experimental data: for example, by including thermal and viscous losses via complex wavenumber. Furthermore, the variation in the amplitude fitting parameter a_1 indicates that the DELTAEC simulations should be tuned to each trial individually in future work.

Figure 5 shows a comparison between the amplitude of the experimentally measured acoustic pressure signal, p_{exp}, and the estimated (fitted) sinusoidal waveforms, $\hat{p}_{\text{exp}}$ and $\hat{\bar{p}}_{\text{sim}}$. Each chart represents the results from one experimental trial with a prescribed relative speaker driver phasing. The waveforms are cropped such that only the region $x_A < x < x_B$ is shown; i.e., the secondary chambers before and after the speakers are excluded in the graphs. The four color-coded circular markers show the amplitudes of the signals measured by each of the microphones at their respective positions. The black solid and dashed lines show the fitted experimental pressure waveforms: i.e., real and imaginary parts of $\hat{p}_{\text{exp}}(x,0)$. In all six cases, the real part of the fit, $\Re[\hat{p}_{\text{exp}}]$, is in good agreement with the microphone data. The fitted sinusoids for the DELTAEC simulation results are shown as purple solid and dashed lines for the real and imaginary parts of $\hat{\bar{p}}_{\text{sim}}(x,0)$, respectively. There is generally a good agreement between $\Im[\hat{\bar{p}}_{\text{sim}}]$ and $\Im[\hat{\bar{p}}_{\text{exp}}]$ for the cases shown, despite the large magnitude of δ_{exp}.

A more visually useful comparison of the simulation results and experimental measurements is shown in Fig. 6 for the same six cases of Fig. 5. The title of each subplot

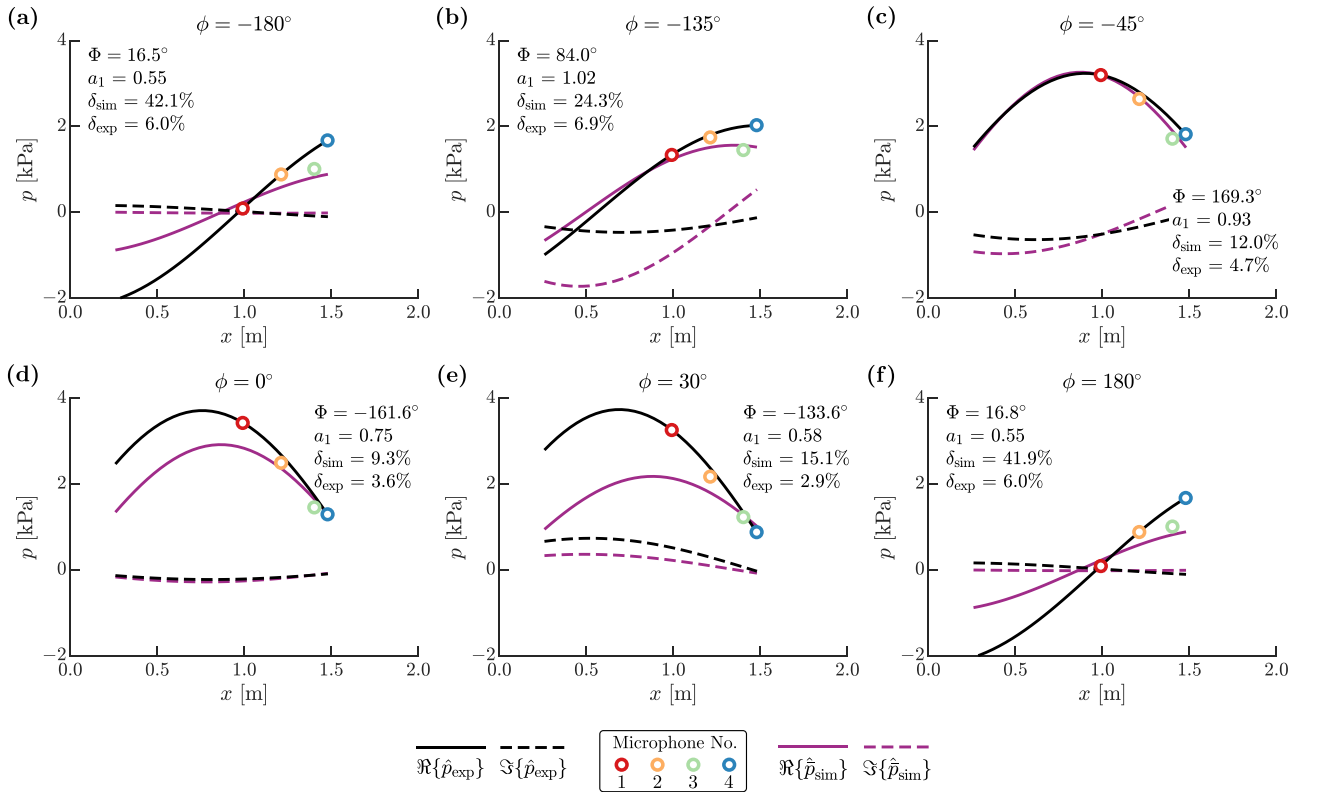

FIG. 5. (Color online) Estimated pressure waveform fit of DELTAEC simulation results, $\hat{\bar{p}}_{\text{sim}}$, and estimated experimental pressure waveform, $\hat{p}_{\text{exp}}$. Experimental pressure amplitude values, p_{exp}, are shown as circular markers. The real part of the estimated waveforms are purple solid lines for DELTAEC output and black solid lines for experimental data. The imaginary parts are dashed lines with the same color scheme. The text on each chart indicates the absolute time phase shift, Φ, the amplitude adjustment, a_1, for the simulated data, the simulation estimation error, δ_{sim}, and the experimental estimation error, δ_{exp}. The relative driver phase difference associated with each experimental trial is shown in the title of each case.

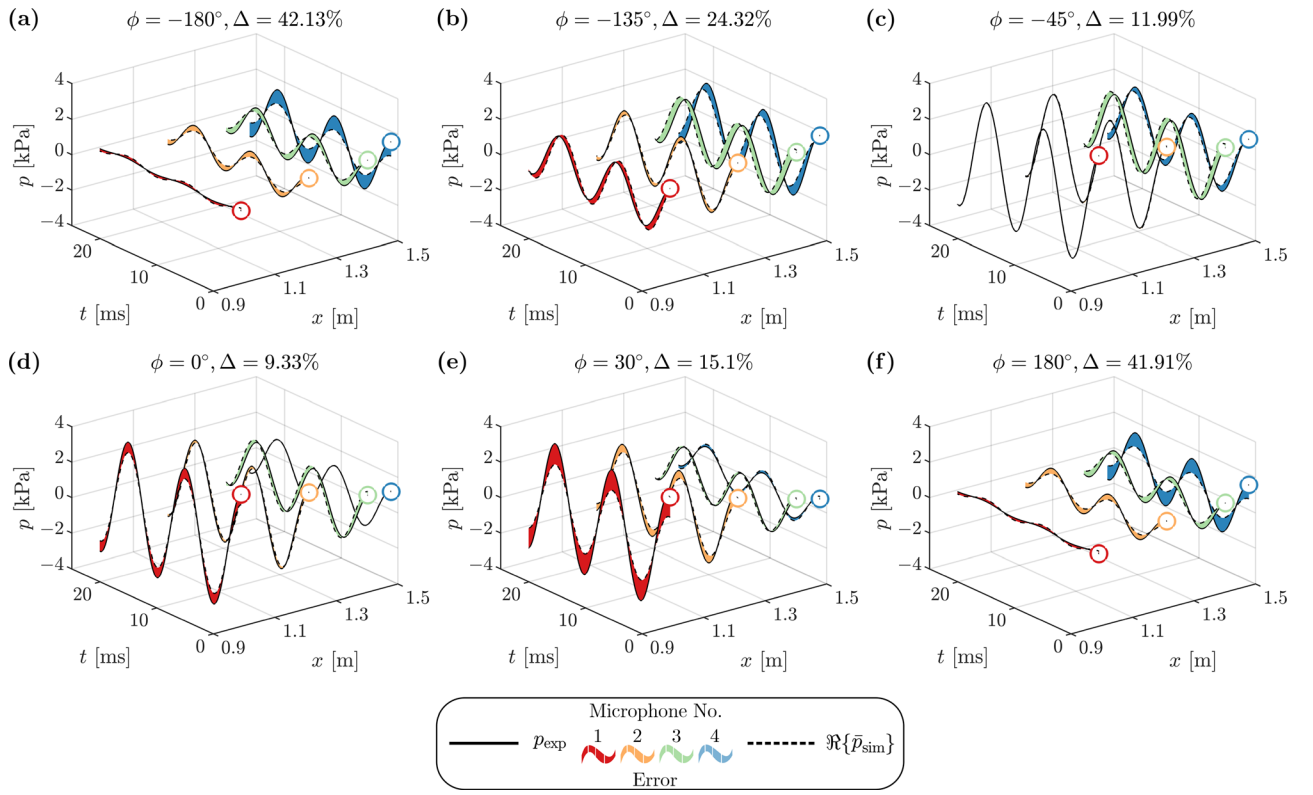

FIG. 6. (Color online) Comparison of the raw microphone signals, p_{exp} (solid), and ideal waveform fit for DELTAEC signals, $\bar{p}_{sim}(x,t)$ (dashed), at each microphone location. The difference between the two curves is filled with a color corresponding to each microphone. The title shows the relative speaker driver phasing (ϕ) and the error between the two signals as a percentage (Δ).

shows the relative speaker driver phase difference, ϕ, and the error, Δ, as defined in Eq. (10). The raw microphone signal is shown as a solid line, and $\Re\{\hat{\bar{p}}_{sim}\}$ values at the four microphone locations are shown as a dashed black line. The space between the two curves is colored according to the microphone index. The spatial location x and time point t are shown on the horizontal axes, and the pressure amplitude in kilopascals is shown on the vertical one. In general, Fig. 6 serves to illustrate that the overall behavior of the experimental TARDE system is well captured by the simulation results and provides for some qualitative understanding of the error metric Δ.

Finally, the same curves from Fig. 6 are collapsed back into 2D space and shown in Fig. 7 to illustrate the discrepancy in time phasing between the simulation and experiment. The $\phi = -135°$ in Fig. 7(b) shows that there is a substantial shift in time between the simulation and experiment. The cause of this discrepancy is due to the difference in the predicted traveling-wave nature of the system. When the four microphone signals are perfectly aligned in time, as in Figs. 7(a) and 7(f), a pure standing wave is expected. In the other case, when each microphone reads a pressure maximum at a different point in time—such as in Fig. 7(b)—a more traveling-wave-like behavior is expected. Conceptually, when the traveling-wave peak travels through the tube, each microphone measures it at a later time than the previous one. In the case of $\phi = -135°$, in Fig. 7(b), the DELTAEC model predicts a wave that is mostly traveling: when microphone 4 measures an absolute minimum, microphone 1 is about 75% of its minimum—contrast this with Fig. 7(a), where the minima are almost all aligned. The experimental data, however, predict a wave that has a lower eccentricity, i.e., one that is closer to a standing wave. This discrepancy cannot be affected by any of the fitting or optimization procedures, so it shows as a large error. This effect is especially apparent in Fig. 7(b), where the model predicts a large eccentricity, but the experimental data show a less traveling-wave-like response. The fact that the experimental microphone readings show an eccentricity that is more or less traveling-wave-like than anticipated (from the simulations) is most likely due to the imperfect nature of the moving-coil drivers. In cases where there is more net force acting on each speaker, such as $\phi = -135°$ in Fig. 7(b), the speaker is incapable of maintaining its intended position. This is evidence of one fundamental challenge of using moving-coil speakers with limited driving amplitude and rigidity to create traveling waves.

C. Traveling wave synthesis

The final results of the investigation into static driver phase lag are shown in Fig. 8. The simulation results in Figs. 8(a) and 8(b) are shown for the full range of speaker phase differences from $-180°$ to $180°$, and the experimental validation points are shown for 25 cases. The wave eccentricity values, denoted by $e_{c,sim}$ and $e_{c,exp}$, are computed using the estimated waveform coefficients $W_{\pm,sim}$ and

https://doi.org/10.1121/10.0023954

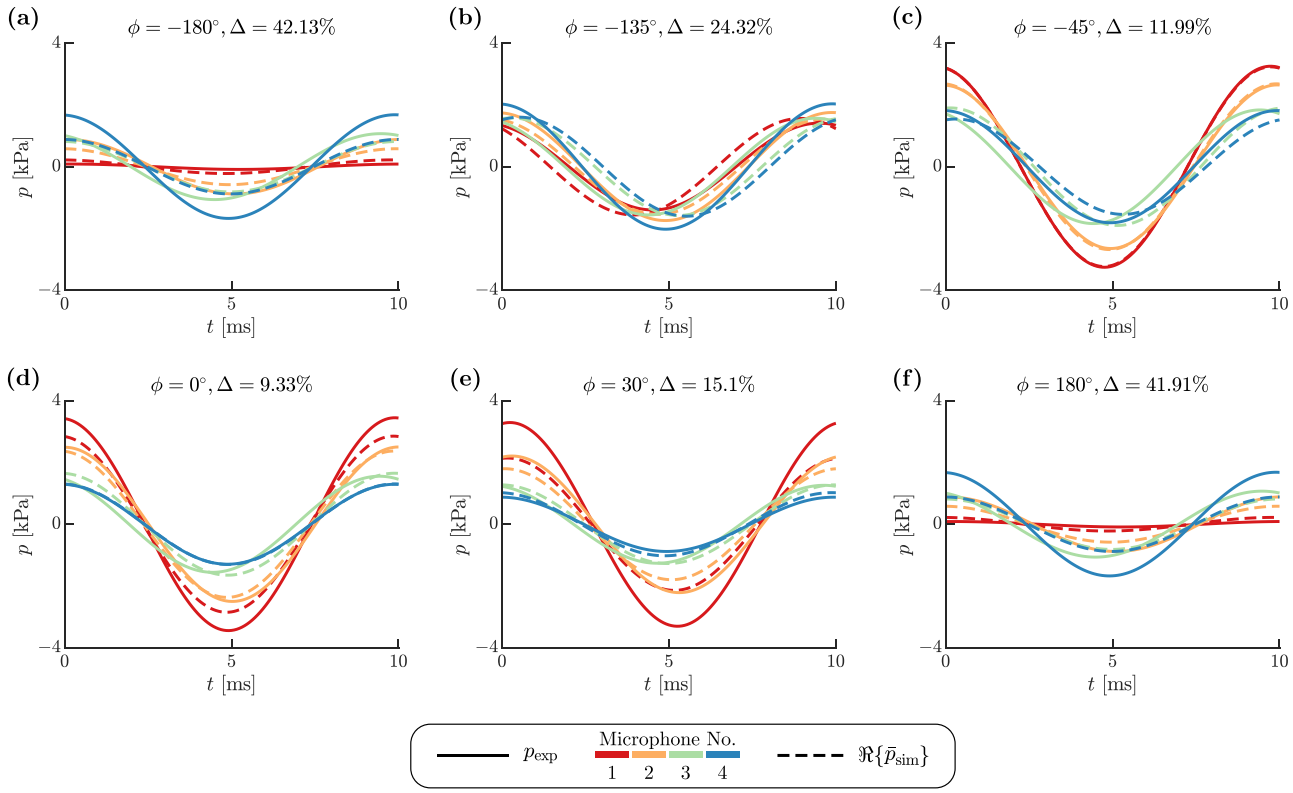

FIG. 7. (Color online) Simulated and experimentally measured acoustic pressure results overlaid. The solid curves represent p_{exp}, while the dashed curves represent $\Re\{\bar{p}_{\text{sim}}\}$. The title shows the relative speaker driver phasing (ϕ) and the error as a percentage (Δ).

$W_{\pm,\text{exp}}$ for the simulation and experimentally obtained data, respectively, and are shown in Fig. 8(b) to be in good agreement considering the challenges with synthesizing a traveling wave with semi-rigid dynamic boundaries. It is important to note the different y axis scales for the simulation and experimental data sets: the experiment showed much lower magnitude eccentricity (and thus more standing-wave-like behavior) in most cases, but the trend in the data is in excellent agreement with the simulation. The results of Fig. 8(b) prove that the two driver system does function as intended and creates a traveling acoustic wave within the resonator. As discussed in Sec. II A, the magnitude of the eccentricity indicates the level of traveling-wave-like behavior, with $|e_c| = 1$ indicating a pure traveling wave. Figure 8 implies that the temperature difference across the stack is maximized when the speaker phase lag is $\phi = 60°$. This case showed a larger pressure amplitude than cases with greater eccentricity, which likely increased the temperature difference. These results indicate that the temperature difference can be directly controlled by the phase lag of the speakers and that it is directly correlated with the wave eccentricity. Further differences between measured and simulated values are likely due to uncertainty from the experimental apparatus and measurement error in addition to differences in the acoustic dynamics. For example, the thermocouples were in contact with the stack as best as could reasonably be achieved, but not perfectly. In addition, irregular porosity around the edges of the stack from

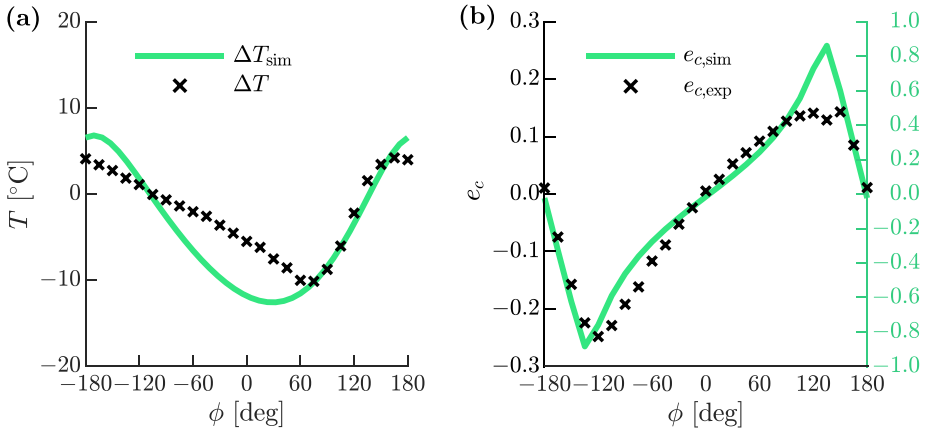

FIG. 8. (Color online) Performance as a function of speaker driver phase difference ϕ. (a) Temperature difference across stack with green line from DELTAEC parametric simulation (ΔT_{sim}) and cross-markers from experimental data (ΔT). (b) Wave eccentricity variation with solid line from DELTAEC simulation ($e_{c,\text{sim}}$) and cross-markers from experimental data ($e_{c,\text{exp}}$).

rough cutting and changes in the diameter and material of the TARDE walls near the stack are other possible sources of difference in temperature behavior.

D. Open-loop temperature difference control

Given the tunability of the stack temperatures and their response to phase changes illustrated earlier, the notion of obtaining a desired temperature ($T_{1,\mathrm{des}}$ and $T_{2,\mathrm{des}}$) by varying the relative driver phase should be possible. As a final step, we tested the TARDE system's ability to track the temperature under open-loop control. Figure 9 shows the desired temperature values for the two temperature sensors. The red dashed line shows the desired temperature for the near side (T_1 at x_s), and the blue dashed line shows the desired temperature for the far side (T_2 at $x_s + L_s$). The solid red and blue lines show the filtered versions of the experimentally obtained temperature readings for the near and far sides, respectively. A set of four desired temperature differences were selected, and the driver phase difference required to obtain those temperature differences were selected based on the data in Fig. 8(a). As shown in Fig. 9(a), the TARDE is capable of tracking the temperature difference, including the switch between the hot and cold sides, very effectively. This result indicates that the temperature variation in the TARDE is a function of the relative driver phases, which can be tuned to provide the desired temperature difference across the two sensors. Additionally, as shown in Fig. 9(b), the value of the pressure amplitude at the various microphone locations specifically changes at the time stamps corresponding to a change in the desired temperature, indicating that the net acoustic pressure wave changes instantaneously within the TAR but the temperature difference across the two sides changes at a relatively slower pace. Because the system operates at steady state, the wave eccentricity in the regions of constant desired temperature in Fig. 9(a) can be found from the corresponding cases in Figs. 8(a) and 8(b).

V. CONCLUSION

This work has shown, through both simulation and experimental results, the ability to control the temperature difference across a thermoacoustic stack in real time by employing two speaker drivers to create dynamic boundary conditions that alter the time-phasing and wave dynamics in the resonator. An experimental apparatus was constructed such that two moving-coil speakers, used as end caps but also equipped with a secondary chamber behind each speaker to equalize the pressure with that of the working mean pressure along the length of the resonator, would excite an acoustic wave in a cylindrical tube. A Celcor ceramic stack inserted in a fixed location was shown to exhibit a temperature gradient along its length based on the traveling-wave dynamics of the acoustic wave excited by the speakers. Microphone measurements taken during testing verified that the wave eccentricity, a measure of the similarity of the pressure wave to a pure standing or traveling wave, varied with the speaker driver phasing. DELTAEC simulations were in good agreement overall with the experimental measurement in terms of both the acoustic dynamics and the temperature difference across the stack. By adjusting the relative phase lag between the two speakers, the temperature gradient across the stack could be made to increase, decrease, or even change sign such that the cold side nearest

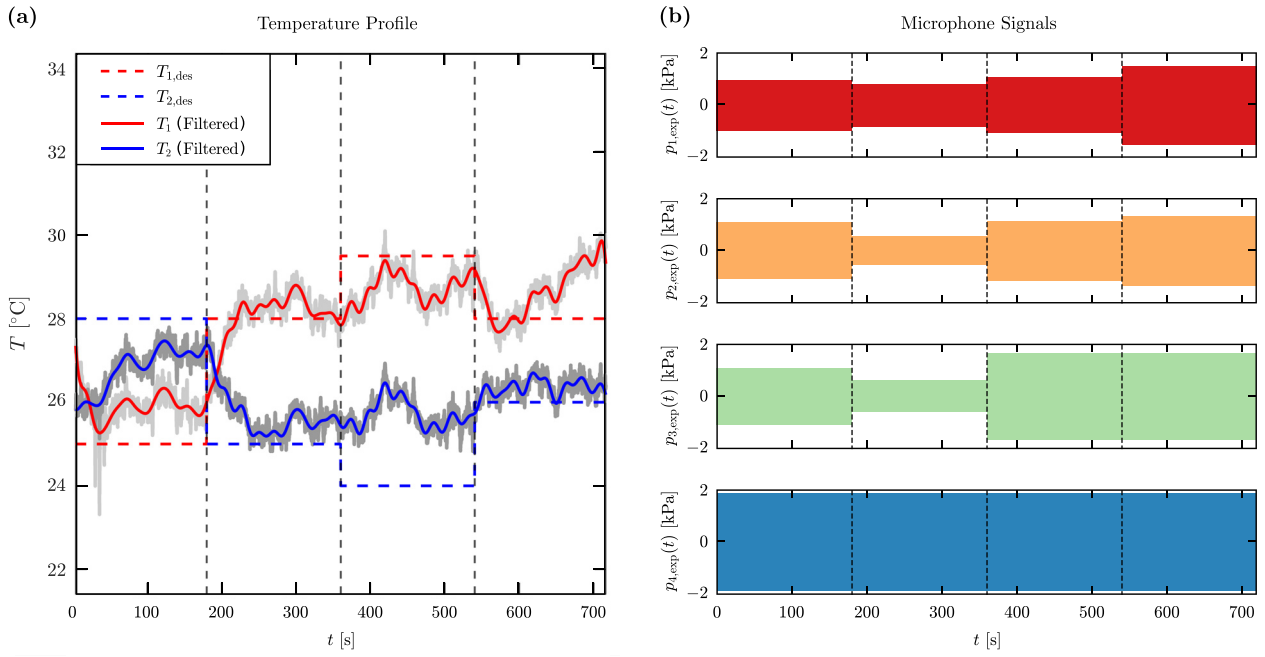

FIG. 9. (Color online) Temperature readings and microphone signals for temperature tracking. (a) shows the tracked (solid, T_1 and T_2) and desired (dashed, $T_{1,\mathrm{des}}$ and $T_{2,\mathrm{des}}$) temperature values. T_1 ($T_{1,\mathrm{des}}$) and T_2 ($T_{2,\mathrm{des}}$) are color coded as red and blue solid (dashed) lines, respectively. (b) shows the four microphone signals recorded while tracking the desired temperature. The dashed black lines indicate the time of phase change. These are set at $t = 180$ s, $t = 360$ s, and $t = 540$ s.

https://doi.org/10.1121/10.0023954

the center of the tube became the hot side. Finally, a desired temperature difference that changes in time was achieved through phase control adding to the functionality of the shown TAR system. Future work investigating a variation in the transducer supply voltage ratio and amplitude would also be of interest; it is possible that energy efficiency could be improved or a more optimal pressure-velocity phasing could be reached by using a lower supply voltage on one transducer. Additional future work of interest includes variation of the stack location and correlating the performance of different speaker phasings with different stack locations—likely a predictable relationship—and investigating subwavelength resonator geometry with actively controlled boundaries. The ability to change the temperature gradient and its direction has important implications for sustainable or remote-location refrigeration applications, such as heating or cooling a sensitive instrument that must remain in a fixed location or that needs to adapt to changing cooling requirements.

SUPPLEMENTARY MATERIAL

See supplementary material for the optimized wave fit parameters for both simulation and experimental results, including the complex wave coefficients, eccentricity, and fit error.

ACKNOWLEDGMENTS

The authors acknowledge support of this work by the U.S. National Science Foundation through Award No. 1904254 as well as the Los Alamos National Laboratory's Laboratory Directed Research & Development Program (LDRD). This work was performed at the Sound and Vibrations Laboratory at the University at Buffalo (SUNY) and the Center for Integrated Nanotechnologies operated for the U.S. Department of Energy's Office of Science. Los Alamos National Laboratory, an affirmative action equal opportunity employer, is managed by Triad National Security, LLC, for the U.S. Department of Energy's NNSA, under Contract No. 89233218CNA000001.

[1]O. G. Symko, E. Abdel-Rahman, Y. Kwon, M. Emmi, and R. Behunin, "Design and development of high-frequency thermoacoustic engines for thermal management in microelectronics," Microelectron. J. **35**(2), 185–191 (2004).
[2]T. J. Flynn, T. A. Fuller, S. Rufener, C. E. A. Finney, and C. S. Daw, "Thermoacoustic vibrations in industrial furnaces and boilers," in *Proceedings of AFRC 2017 Industrial Combustion Symposium*, Houston, TX [American Flame Research Committee (AFRC), Lakewood Ranch, FL, 2017].
[3]L. Zhang, J. Hu, Z. Wu, E. Luo, J. Xu, and T. Bi, "A 1 kW-class multi-stage heat-driven thermoacoustic cryocooler system operating at liquefied natural gas temperature range," Appl. Phys. Lett. **107**(3), 033905 (2015).
[4]M. Tijani and S. Spoelstra, "Study of a coaxial thermoacoustic-stirling cooler," Cryogenics **48**(1–2), 77–82 (2008).
[5]M. A. Timmer, K. de Blok, and T. H. van der Meer, "Review on the conversion of thermoacoustic power into electricity," J. Acoust. Soc. Am. **143**(2), 841–857 (2018).
[6]G. Chen, L. Tang, B. Mace, and Z. Yu, "Multi-physics coupling in thermoacoustic devices: A review," Renew. Sustain. Energy Rev. **146**, 111170 (2021).
[7]M. Nouh, O. Aldraihem, and A. Baz, "Piezo-driven thermoacoustic refrigerators with dynamic magnifiers," Appl. Acoust. **83**, 86–99 (2014).
[8]S. L. Garrett, J. A. Adeff, and T. J. Hofler, "Thermoacoustic refrigerator for space applications," J. Thermophys. Heat Transfer **7**(4), 595–599 (1993).
[9]T. J. Hofler, *Thermoacoustic Refrigerator Design and Performance (Heat Engine, Resonator, Microphone)* (University of California, San Diego, 1986).
[10]B. Moore, J. Zan, B. Hannah, T. Chui, K. Penanen, and M. Weilert, "Mid infrared instrument cooler subsystem test facility overview," IOP Conf. Ser. Mater. Sci. Eng. **278**, 012006 (2017).
[11]M. Petach and M. Michaelian, "Mid InfraRed Instrument (MIRI) cooler cold head assembly acceptance testing and characterization," in *18th International Cryocooler Conference, ICC 18*, Boulder, CO (ICC Press, Boulder, CO, 2014), pp. 11–17.
[12]R. Ross, Jr., "Conceptual design and development history of the MIRI cryocooler system on JWST," in *22nd International Cryocooler Conference, ICC 22*, Bethlehem, PA (ICC Press, Boulder, CO, 2022).
[13]G. W. Swift, "Thermoacoustic engines," J. Acoust. Soc. Am. **84**(4), 1145–1180 (1988).
[14]G. W. Swift, *Thermoacoustics: A Unifying Perspective for Some Engines and Refrigerators* (Springer, New York, 2002).
[15]R. Raspet, J. Brewster, and H. E. Bass, "A new approximation method for thermoacoustic calculations," J. Acoust. Soc. Am. **103**(5), 2395–2402 (1998).
[16]T. J. Hofler, "Performance of a short parallel-plate thermoacoustic stack with arbitrary plate separation," J. Acoust. Soc. Am. **88**(S1), S94 (1990).
[17]C. Desjouy, G. Penelet, and P. Lotton, "Active control of thermoacoustic amplification in an annular engine," J. Appl. Phys. **108**(11), 114904 (2010).
[18]C. Olivier, G. Penelet, G. Poignand, and P. Lotton, "Active control of thermoacoustic amplification in a thermo-acousto-electric engine," J. Appl. Phys. **115**(17), 174905 (2014).
[19]J. P. Epperlein, B. Bamieh, and K. J. Åström, "Control laboratory experiments in thermoacoustics using the Rijke tube," in *2014 American Control Conference*, Portland, OR (IEEE, New York, 2014), pp. 2550–2556.
[20]J. Smoker, M. Nouh, O. Aldraihem, and A. Baz, "Energy harvesting from a standing wave thermoacoustic-piezoelectric resonator," J. Appl. Phys. **111**(10), 104901 (2012).
[21]M. Nouh, O. Aldraihem, and A. Baz, "Energy harvesting of thermoacoustic-piezo systems with a dynamic magnifier," J. Vib. Acoust. **134**(6), 061015 (2012).
[22]M. Nouh, O. Aldraihem, and A. Baz, "Theoretical modeling and experimental realization of dynamically magnified thermoacoustic-piezoelectric energy harvesters," J. Sound Vib. **333**(14), 3138–3152 (2014).
[23]A. Roshwalb, M. Nouh, O. Aldraihem, and A. Baz, "Performance of a traveling wave thermoacoustic-piezoelectric energy harvester: An electrical circuit analogy approach," J. Intell. Mater. Syst. Struct. **25**(11), 1372–1383 (2014).
[24]M. Nouh, O. Aldraihem, and A. Baz, "Onset of oscillations in traveling wave thermo-acoustic-piezo-electric harvesters using circuit analogy and spice modeling," J. Dyn. Syst. Meas. Control **136**(6), 061005 (2014).
[25]M. Nouh, O. Aldraihem, and A. Baz, "Optimum design of thermoacoustic-piezoelectric systems with dynamic magnifiers," Eng. Optim. **46**(4), 543–561 (2014).
[26]G. W. Swift, "Thermoacoustic engines and refrigerators," Phys. Today **48**(7), 22–28 (1995).
[27]J. Callanan and M. Nouh, "Optimal thermoacoustic energy extraction via temporal phase control and traveling wave generation," Appl. Energy **241**, 599–612 (2019).
[28]T. L. Shearer, H. F. Hofmann, R. W. Smith, and S. L. Garrett, "Sensorless control of a thermoacoustic refrigerator," J. Acoust. Soc. Am. **116**(1), 288–293 (2004).
[29]G. Poignand, B. Lihoreau, P. Lotton, E. Gaviot, M. Bruneau, and V. Gusev, "Optimal acoustic fields in compact thermoacoustic refrigerators," Appl. Acoust. **68**(6), 642–659 (2007).
[30]I. A. Ramadan, H. Bailliet, G. Poignand, and D. Gardner, "Design, manufacturing and testing of a compact thermoacoustic refrigerator," Appl. Therm. Eng. **189**, 116705 (2021).

[31]G. Chen and J. Xu, "Active control of heat transport inside the porous material of a looped-tube dual-acoustic-driver thermoacoustic refrigerator," Cryogenics **125**, 103516 (2022).
[32]A. Widyaparaga, T. Hiromatsu, Deendarlianto, M. Kohno, and Y. Takata, "Acoustic field alteration in a 100Hz dual acoustic driver straight tube travelling wave thermoacoustic heat pump for thermoacoustic heat transport control," Int. J. Heat Mass Transfer **151**, 119274 (2020).
[33]A. Widyaparaga, T. Hiromatsu, T. Koshimizu, D. Deendarlianto, M. Kohno, and Y. Takata, "Thermoacoustic heat pumping direction alteration by variation of magnitude and phase difference of opposing acoustic waves," Appl. Therm. Eng. **101**, 330–336 (2016).
[34]N. Rott, "Damped and thermally driven acoustic oscillations in wide and narrow tubes," J. Appl. Math. Phys. (ZAMP) **20**(2), 230–243 (1969).
[35]M. A. Nouh, N. M. Arafa, and E. Abdel-Rahman, "Stack parameters effect on the performance of anharmonic resonator thermoacoustic heat engine," Arch. Mech. Eng. **61**(1), 115–127 (2014).
[36]L. Kinsler, A. R. Frey, and A. B. Coppens, *Fundamentals of Acoustics*, 4th ed. (Wiley, Hoboken, NJ, 2000).
[37]I. Bucher, "Estimating the ratio between travelling and standing vibration waves under non-stationary conditions," J. Sound Vib. **270**(1), 341–359 (2004).
[38]J. P. Clark, W. C. Ward, and G. W. Swift, "Design environment for low-amplitude thermoacoustic energy conversion (DeltaEC)," J. Acoust. Soc. Am. **122**(5), 3014 (2007).
[39]B. Ward, J. Clark, and G. Swift, *Design Environment for Low-Amplitude Thermoacoustic Energy Conversion, DELTAEC Version 6.2: Users Guide* (Los Alamos National Laboratory, Los Alamos, NM, 2008).